

This is a repository copy of *Direct Visualization of Native Defects in Graphite and Their Effect on the Electronic Properties of Bernal-Stacked Bilayer Graphene*.

White Rose Research Online URL for this paper:

<https://eprints.whiterose.ac.uk/178041/>

Version: Published Version

Article:

Joucken, Frédéric, Velasco Jr, Jairo, Ferreira, Aires orcid.org/0000-0001-6017-8669 et al. (1 more author) (2021) Direct Visualization of Native Defects in Graphite and Their Effect on the Electronic Properties of Bernal-Stacked Bilayer Graphene. *Nano Letters*. pp. 7100-7108. ISSN 1530-6984

Reuse

Items deposited in White Rose Research Online are protected by copyright, with all rights reserved unless indicated otherwise. They may be downloaded and/or printed for private study, or other acts as permitted by national copyright laws. The publisher or other rights holders may allow further reproduction and re-use of the full text version. This is indicated by the licence information on the White Rose Research Online record for the item.

Takedown

If you consider content in White Rose Research Online to be in breach of UK law, please notify us by emailing eprints@whiterose.ac.uk including the URL of the record and the reason for the withdrawal request.


Direct Visualization of Native Defects in Graphite and Their Effect on the Electronic Properties of Bernal-Stacked Bilayer Graphene

Frédéric Joucken,* Cristina Bena,* Zhehao Ge, Eberth Quezada-Lopez, Sarah Pinon, Vardan Kaladzhyan, Takashi Taniguchi, Kenji Watanabe, Aires Ferreira, and Jairo Velasco Jr.*


 Cite This: *Nano Lett.* 2021, 21, 7100–7108

 Read Online

ACCESS |

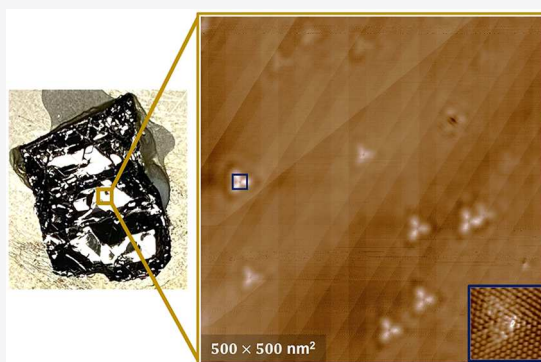
 Metrics & More

 Article Recommendations

 Supporting Information

ABSTRACT: Graphite crystals used to prepare graphene-based heterostructures are generally assumed to be defect free. We report here scanning tunneling microscopy results that show graphite commonly used to prepare graphene devices can contain a significant amount of native defects. Extensive scanning of the surface allows us to determine the concentration of native defects to be $6.6 \times 10^8 \text{ cm}^{-2}$. We further study the effects of these native defects on the electronic properties of Bernal-stacked bilayer graphene. We observe gate-dependent intravalley scattering and successfully compare our experimental results to T-matrix-based calculations, revealing a clear carrier density dependence in the distribution of the scattering vectors. We also present a technique for evaluating the spatial distribution of short-scale scattering. Finally, we present a theoretical analysis based on the Boltzmann transport equation that predicts that the dilute native defects identified in our study are an important extrinsic source of scattering, ultimately setting the charge carrier mobility at low temperatures.

KEYWORDS: *Bilayer graphene, graphite, scanning tunneling microscopy, quasiparticle interference, dopant*

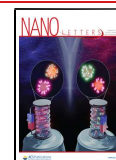


INTRODUCTION

In the early days of graphene research, when transport experiments were carried out on graphene supported by SiO_2 , significant attention was devoted to understanding the effects of charge impurities in graphene samples. Notably, the minimum conductivity was measured to be close to twice the quantum of conductance ($4e^2/h$) in zero magnetic field.^{1–3} This was shown to be an extrinsic property of graphene resulting from the inhomogeneous potential landscape created by charged impurities in the supporting SiO_2 .^{4,5} Later, demonstration of ballistic transport in suspended graphene samples^{6,7} and in graphene encapsulated in hexagonal boron nitride (hBN)⁸ shifted the attention away from impurity-induced scattering in graphene samples. For suspended samples, a consensus on the primary role of electron–phonon interaction as limiting the mobility seems to have emerged.^{9,10} For hBN supported samples, magnetotransport experiments on mono-¹¹ and Bernal-stacked bilayer graphene (BLG)¹² have pointed toward intravalley scattering as the dominant factor limiting the electronic mobility on this substrate. The intravalley scattering was attributed to strain-induced pseudo-magnetic fields.^{11,12} More recently, however, the role of localized impurities as scatterers has reemerged in the context of twisted graphene samples, with indications that they might play a key role in these systems.^{13–15}

Interestingly, to the best of our knowledge, there has been so far no report of a scanning tunneling microscopy (STM) study of *native* point-like defects in graphite used for making graphene devices. Trenches and steps^{16–18} as well as grain boundaries^{18–20} have been investigated by STM, but these types of defects are easily avoidable when making devices from exfoliated graphene flakes as they are visible under an optical or an atomic force microscope. Several STM studies have focused on point-like defects in graphite, but all of these were obtained on samples with intentionally induced defects (mostly by ion irradiation).^{21,22} As for graphene, several investigations of native point-like defects have been reported^{23–26} but they were not performed on exfoliated graphene and the influence of these defects on the transport properties was not addressed. The only atomic scale study carried out on exfoliated graphene that focused on the role of localized charged impurities was by Zhang et al.²⁷ It revealed that the impurities were not defects in the graphene lattice but likely molecules trapped between graphene and the supporting

Received: April 13, 2021
Revised: August 15, 2021
Published: August 20, 2021



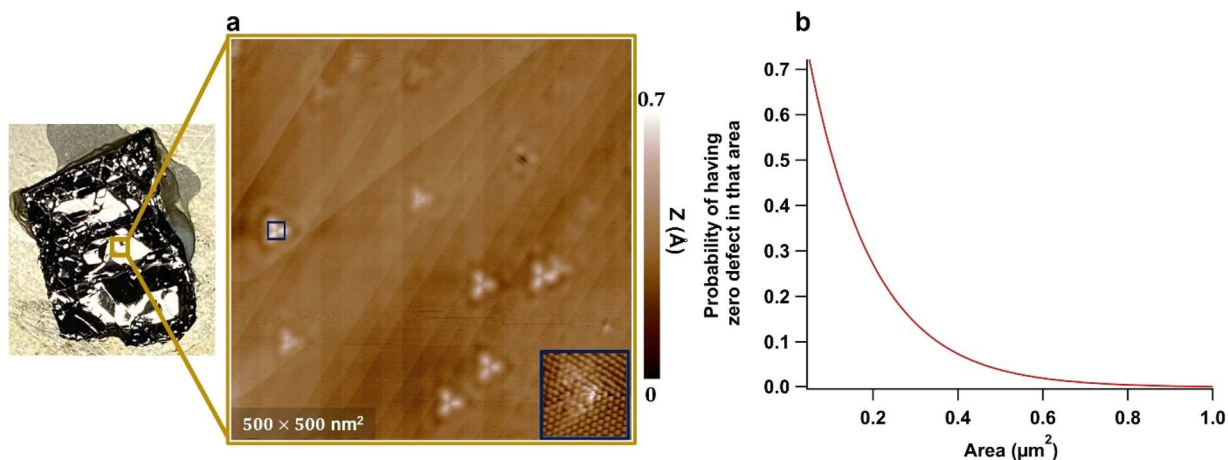


Figure 1. Native defects in graphite. (a) Large-scale ($500 \times 500 \text{ nm}^2$) low-bias (4 mV) scanning tunneling microscopy (STM) topographic image of graphite (“Flaggy Flakes” from NGS Naturgraphit), exfoliated in ultrahigh vacuum moments prior to the STM experiments. Quasiparticle interference (QPI) patterns with triangular symmetry are visible. As discussed in the text, these QPI patterns are attributed to scattering off of atomic scale defects. A zoom-in around one of these defects (blue square) located in the topmost layer is shown in the inset. (b) Probability of having no defect in a monolayer, as a function of the area, assuming a defect concentration of $(6.6 \pm 2) \times 10^8 \text{ cm}^{-2}$.

SiO_2 , a substrate that has become nearly obsolete for electronic devices since the advent of hBN for this role. The absence of direct experimental evidence for the presence of native defects in graphene devices and in graphite parent crystals likely explains why the role of defects in the transport properties of graphene devices has been thus far mostly overlooked.

Here we report STM results that establish the presence of atomic-scale defects in a type of graphite commonly used to make graphene devices with the standard exfoliation technique. We further characterize the effects of these defects on the electronic properties of BLG. By mapping quasiparticle scattering interference (QPI) on mesoscopic areas (typically greater than $300 \times 300 \text{ nm}^2$), we visualize the intervalley scattering patterns induced by quasiparticles scattered off localized defects. We compare our experimental QPI results to T-matrix-based calculations and reveal the dramatic influence of the charge carrier density and the perpendicular electric field (tuned by the gate voltage) on the distribution of the scattering vectors. We also study the spatial extension of intervalley scattering induced by the same localized defects and show that it extends significantly ($>10 \text{ nm}$) away from them, following patterns that resemble the intervalley scattering patterns produced around the same defects. Subtle differences between the inter- and the intervalley patterns are however observed and explained. Finally, we present a theoretical analysis based on the Boltzmann transport equation that strongly indicates that, despite their low concentration, the native defects we have observed become the dominant source of scattering at low temperature.

Several factors enabled our discovery of native defects in graphite crystals that are commonly used for mechanical exfoliation but were so far unreported. It was important to image numerous large areas (typically greater than $200 \times 200 \text{ nm}^2$) at low tip-sample bias (few mVs) and at relatively high current (typically 1–2 nA; sometimes greater, depending on the tip state). For the experiments performed on devices, using a BLG sample enhanced the visibility of the QPI patterns compared to the monolayer case. We attribute this to the scattering selection rules being less favorable for producing visible patterns for monolayer graphene.^{28,29}

■ NATIVE DEFECTS IN GRAPHITE

Figure 1a shows a typical large-scale ($500 \times 500 \text{ nm}^2$) low-bias (4 mV) STM topographic image of a freshly exfoliated graphite crystal (“Flaggy Flakes” from NGS Naturgraphit; we obtained similar results on “Graphenium Flakes” from the same company). On this image, several localized triangular patterns can be distinguished. By zooming in on each of these patterns and acquiring atomically resolved images with our STM, we found that 20–30% of the triangular patterns observed on large scale images had a localized atomic-scale defect located at their center, in the topmost layer. Such an atomic scale defect is shown in the inset of Figure 1 (other representative defects are shown in the Supporting Information, section I). The nature of most of these defects remains unknown, but we tentatively identify a few of them as nitrogen dopants (see Supporting Information section I). The 20–30% of triangular patterns that were found to have an atomic scale defect at their center (in the topmost layer) appeared the brightest on the large-scale images. From this, we conclude that 70–80% of the patterns that appear on large scale images are produced by atomic scale defects located in buried layers. By counting the total number of defects found on the topmost layer of freshly exfoliated graphite, we determine the defect concentration to be $(6.6 \pm 2) \times 10^8 \text{ cm}^{-2}$ per layer (see Supporting Information section II for details on the counting and uncertainty). Such a concentration of native defects, albeit seemingly low, makes it challenging to fabricate devices which are defect free. We plot in Figure 1b the probability of having no defect in a monolayer as a function of the area, assuming a uniform and random distribution of defects and considering the concentration we have measured (details in Supporting Information section II). One can see that to have a reasonable chance of attaining a defect-free monolayer sheet, areas smaller than $\sim 0.2 \mu\text{m}^2$ should be considered. This becomes even more stringent when considering multilayer samples.

Having established the presence of native defects in the graphite parent crystal, we now move on to study the effects these defects impart on the electronic properties of a back-gated BLG device made from the same parent crystal shown in Figure 1a.

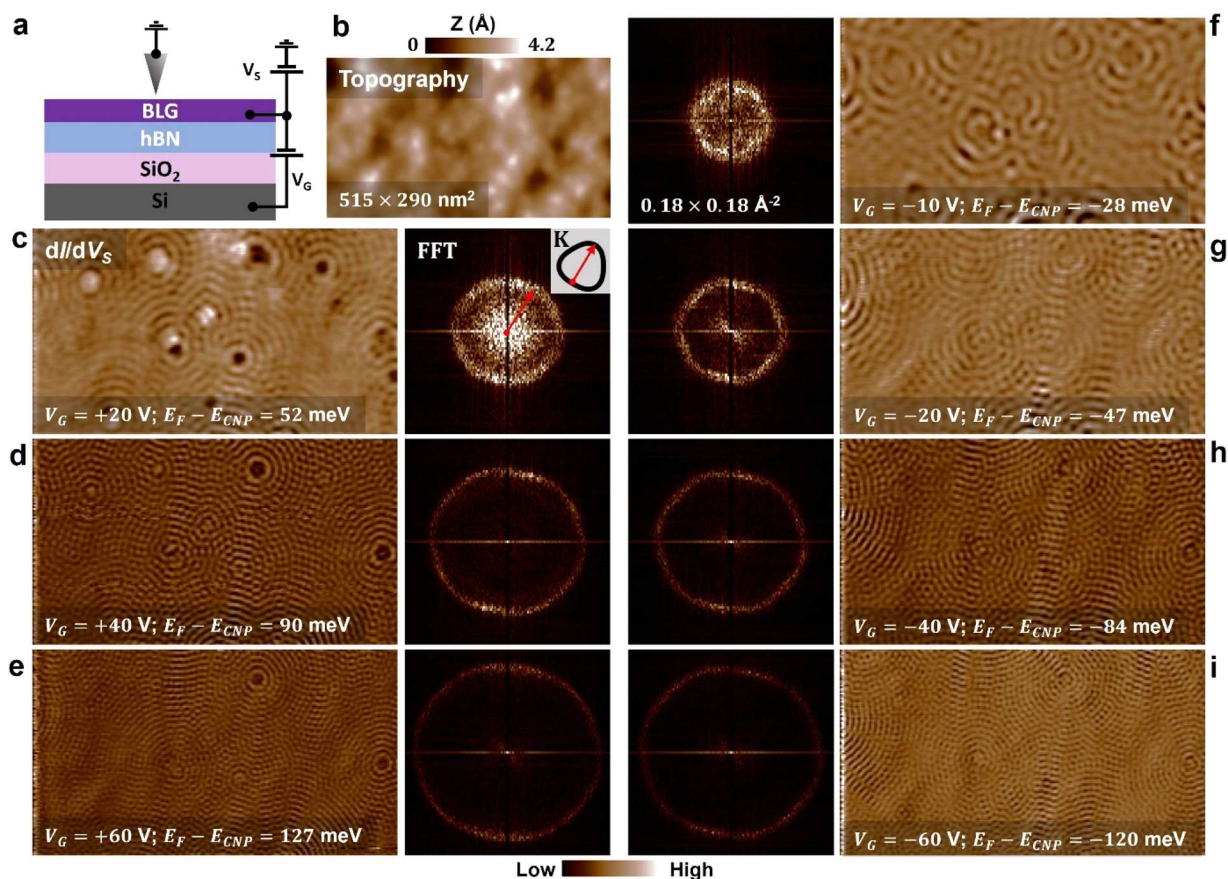


Figure 2. Intravalley scattering in gate tunable Bernal-stacked bilayer graphene (BLG). (a) Schematics of the experimental setup. A back-gated BLG flake atop a ~ 20 nm thick hBN flake is scanned with the STM. (b) Large-scale (515×290 nm 2) topographic STM image of a clean BLG area. (c–i) dI/dV_S maps (3 mV excitation) acquired over the same area as in (b) at various gate voltages (V_G ; indicated), at low sample bias (+5 mV; $I = 0.5$ nA), essentially mapping the local density of states at the Fermi level. The difference between the Fermi level (E_F) and the charge neutrality point (E_{CNP}) is indicated for each gate voltage. The fast Fourier transform (FFT) of each map is also shown (all the FFTs are plotted on the same z -scale). Clear intravalley scattering (schematized in the inset of (c)) pattern is visible both in real space and in the FFT. Whereas all FFT patterns show stronger intensity at the edge of the pattern (empty circles), the FFT pattern at $V_G = +20$ V displays strong intensities for small momentum transfer. This is discussed further in the text in connection with Figure 3.

■ NATIVE DEFECTS IN BLG

We assembled BLG/hBN heterostructures that were deposited on SiO $_2$ /Si (see Methods), with the doped silicon substrate serving as an electrostatic gate; a schematic of the device is shown in Figure 2a. Before analyzing the scattering induced by the dopants in our BLG/hBN heterostructure, we point out that we measured a defect concentration in graphene/hBN devices of $(2.2 \pm 0.7) \times 10^9$ cm $^{-2}$ per layer (see Supporting Information section II for details on the counting and uncertainty; graphene devices include bilayer and multilayer graphene), significantly greater than the defect concentration measured on the freshly exfoliated graphite parent crystal. Thus, it appears that our sample making procedure (see Methods), which involves heating the graphene on hBN stacks in forming gas (Ar/H $_2$) as well as prolonged annealing of the devices in ultrahigh vacuum at 400 °C, results in the creation of additional defects. These two annealing steps are commonly used by researchers studying graphene samples in UHV. We also note that for the BLG/hBN sample, we have counted a number of defects on the top layer which was somewhat smaller than half of the total number of defects (determined by counting the large-scale intravalley scattering patterns). This suggests that defects in the hBN substrate³⁰ or impurities trapped between the hBN and the BLG might be responsible

for some of the intravalley scattering patterns that we have observed. To our knowledge, the only other report of imaging native defects in graphene devices was by Halbertal et al.,³¹ who reported much smaller native defects concentration than what we report here (they saw three defects in a 4×4 μm^2 area, corresponding to 1.9×10^7 cm $^{-2}$). We note however that the technique they used (scanning nanothermometry on encapsulated graphene) is less direct than STM and the effect they attributed to atomic scale defects could have been produced by defects complexes or trapped impurities. We also note that the graphite parent crystal used was not indicated in their study.

■ INTRAVALLEY SCATTERING

Figure 2b shows a topographic STM image of a large (515×290 nm 2) area. Figure 2c–i show dI/dV_S maps acquired in the same region as shown in Figure 2b, at various gate voltages (indicated), together with their corresponding fast Fourier transforms (FFT). Because the tip–sample bias was low (+5 mV), these maps essentially reveal the local density of states at the Fermi level (LDOS(E_F)). The difference between E_F and the charge neutrality point (E_{CNP}) is indicated (see Supporting Information section III for details). Clear QPI patterns (also known as Friedel oscillations) are seen on each of these dI/dV_S

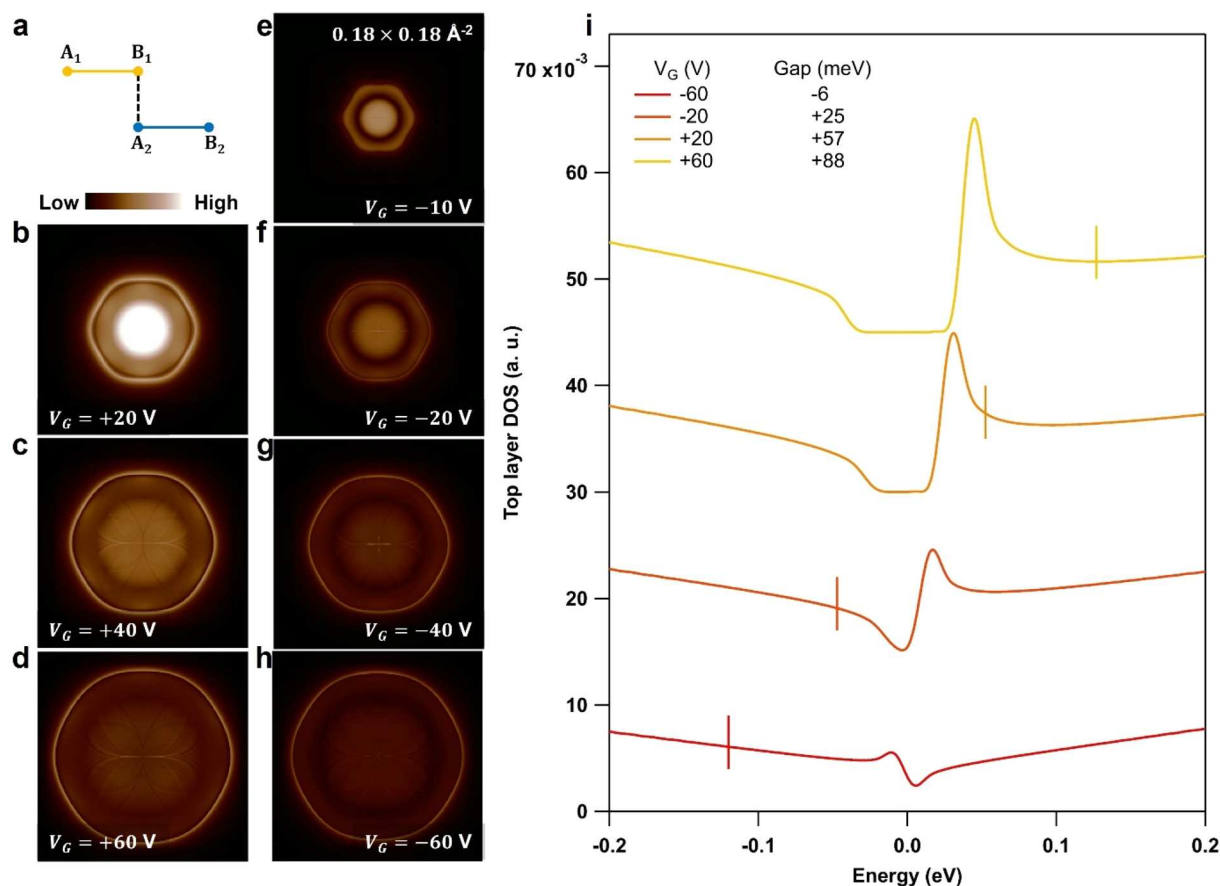


Figure 3. Simulated reciprocal-space signature of defect-induced QPI in gate-tunable BLG. (a) Sublattices in BLG unit cell. (b–h) T-matrix simulations of the QPI in momentum space for the indicated gate voltages. (i) Top-layer density of states (DOS) for the gate voltages indicated. The vertical bar indicates the energy at which the corresponding QPI was acquired (and simulated).

maps. Importantly, these QPI patterns visibly originate from localized scattering centers, as is particularly evident at low gate voltage (panels c and f of Figure 2). The QPI patterns reported in Figure 2 correspond to intravalley scattering (as schematized in the inset of Figure 2c). This appears unambiguously in the FFTs, where the size of the QPI patterns (centered around the origin) have dimensions that correspond to the size of the Fermi surface at the corresponding gate.³² The hexagonal shape of the patterns seen in the FFT is due to the strong trigonal warping of the low energy bands in bilayer graphene.³² We note that the FFT amplitude is for most cases close to zero within the hexagonal boundary of the scattering pattern and maximum at the boundary except for low gate voltages ($V_G = +20$ V and $V_G = -10$ V) where significant intensity is observed for short scattering vectors (small momentum transfer). We also clearly see that the overall amplitude of the FFTs is greater for positive gate voltages than for negative gate voltages (all the FFTs have the same z -scales).

Next, we examine the reciprocal-space signature of the QPI that we obtain from T-matrix simulations^{28,33} and compare it to our experimental results (FFTs in Figure 2). Figure 3b–h shows the simulated FFT for the same doping as in the experiments ($E_F - E_{\text{CNP}}$ indicated in Figure 2), all on the same z -scale. The band gap induced by the perpendicular electric field produced by the backgate and the STM tip is considered in the simulation.^{34–36} The method for determining the values used in the simulation for the band gap and for the electronic doping for each gate voltage is presented in section III of the

Supporting Information. The T-matrix results presented in Figure 3b–h are obtained by averaging the signatures of dopants located on the four atomic sites of the BLG unit cell (A_1 , B_1 , A_2 , and B_2 ; see inset of Figure 3a) and only considering the density of states (DOS) in the top layer (similar to the situation for the STM experiment). The dopant was modeled by an onsite potential of -10 eV (we discuss in the section VI of the Supporting Information the influence of the potential on the QPI signature in real and reciprocal space). One can see that the main features of the experimental FFTs (Figure 2c–i) are captured by the simulations: (i) the overall amplitude of the FFTs is greater for positive gates than for negative ones, and (ii) the spectral weight within the hexagonal pattern, and particularly in the vicinity of the origin (enhancement of small momentum transfer), is greater for smaller gate voltages.

Deeper insight into these two features can be gained by looking at the calculated gate-dependent DOS of the top layer (which is the layer probed by STM). Figure 3i displays the top-layer DOS for pristine BLG computed for four gate voltages of panels b–h. The vertical lines indicate the corresponding position of the Fermi level at these gate voltages (and thus the energy that was probed in the experiments). The values of the gap used to compute these curves are indicated (see Supporting Information section III for the determination of these values). As is observed for the experimental and simulated QPI patterns, an asymmetry between positive and negative gate voltages (feature (i) of the FFTs) is clearly seen

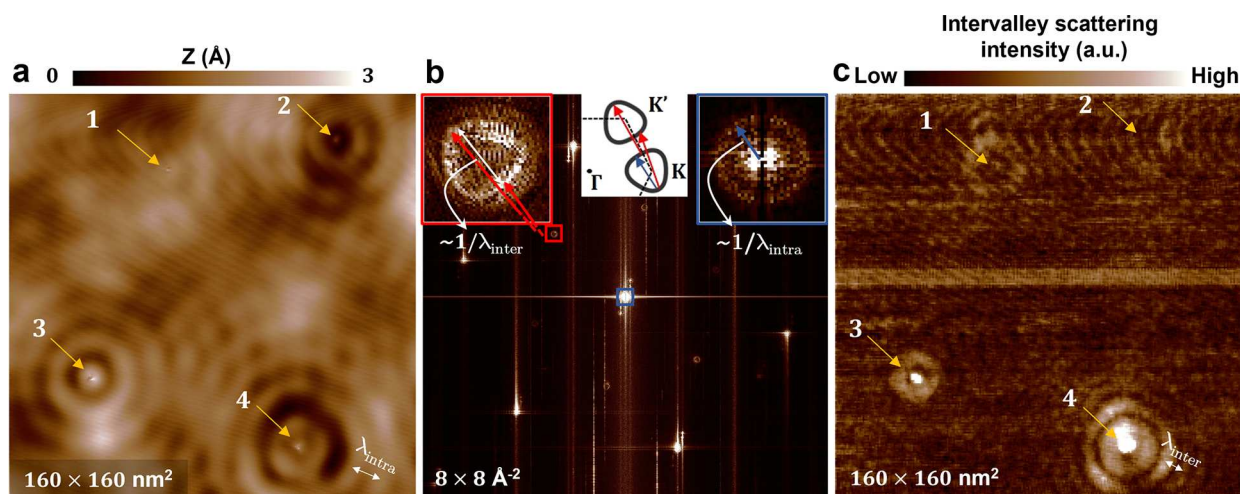


Figure 4. Spatial mapping of intervalley scattering by native defects in BLG. (a) Low-bias (5 mV) high-resolution (2048^2 pixels) STM topographic map of BLG. Four defects are visible (labeled 1–4). Defects 3 and 4 are in the top layer. (b) FFT of (a) of the intervalley scattering (schematized in the inset). Red-boxed inset is a zoom-in around one intervalley scattering feature; the two red arrows indicate extreme intervalley scattering vectors for this pattern. Blue-boxed inset is a zoom-in around the intravalley scattering feature; the blue arrow indicates an extreme intravalley scattering vector. The middle inset illustrates the inter- and intravalley scattering vectors. (c) Intervalley scattering map on the same area as (a) obtained by taking the ratio between the intravalley feature amplitude and the lattice feature amplitude in $2.5 \times 2.5 \text{ nm}^2$ windows in image (a); see main text and [Supporting Information](#) for more details on this computation.

for the top-layer DOS. This asymmetry is due to the polarization of the BLG sheet in the z direction upon application of the electric field induced by the gate and the STM tip. Further asymmetry is produced by the gap closing at $V_G \approx -52 \text{ V}$ rather than $V_G = 0 \text{ V}$. This offset is attributed to the work function mismatch between the tip and the sample.^{35,36}

As a tentative explanation of feature (ii) (enhancement of small momentum transfer for low gate voltages), we first note the proximity of the gap edge in these cases ($V_G = +20 \text{ V}$, $V_G = -10 \text{ V}$, and $V_G = -20 \text{ V}$). However, the precise mechanisms behind this enhancement cannot be explained by pure band structure arguments, as we demonstrate in the [Supporting Information](#) (section VII) by showing computed joint density of states at various gate voltages. The explanation for the enhancement of small momentum transfer at low gate voltage is thus related to the details of the scattering mechanism, such as the overlapping matrix elements between incoming and outgoing states or local modifications of the density of states. These are naturally accounted for in the T-matrix formalism.^{37–40} A close examination of the dI/dV_S map at $V_G = +20 \text{ V}$ (Figure 2c) reveals that the scattering patterns change significantly compared to the other dI/dV_S maps. The wavelike patterns emanating from the point-like scattering centers decay noticeably faster than in the maps taken at higher gate voltages. Also, a high-intensity dI/dV_S signal is observed at the location of some scattering centers. Given the basic properties of Fourier transformation (recall that the Fourier transform of the sinc function is the rectangular function), these features can explain the higher intensity close to the origin in the FFT.

■ INTERVALLEY SCATTERING

Having thoroughly discussed the intravalley scattering caused by native defects, we now investigate the intervalley scattering induced by the same defects in our sample. The intervalley scattering induced by localized defects has already been reported in STM studies on mono- or bilayer graphene.^{23,41,42} However, the spatial extension of the intervalley scattering

away from localized defects has so far lacked attention. In the case of nitrogen dopants for example, the $\sqrt{3} \times \sqrt{3}R30$ pattern associated with intervalley scattering is clearly visible in topographic images near the dopants but seems to quickly ($\sim 1\text{--}2 \text{ nm}$) decay away from the defect.⁴¹ No technique for visualizing the spatial extent of the intervalley scattering induced by point-like defects in graphitic systems has been reported so far. We present below the data and an analysis method that allow us to infer the spatial distribution of the intervalley scattering.

Figure 4a shows a high-resolution (2048×2048 pixels) low-bias (+5 mV) and large-scale ($160 \times 160 \text{ nm}^2$) STM topographic image. Such a map is ideal to study both inter- and intravalley scattering because it captures both the short and long wavelengths associated with the two types of scattering. Several defects are indicated by yellow arrows in Figure 4a. Defects 1 and 2 are buried while defects 3 and 4 are on the top layer (see [Supporting Information](#) section VIII for zoom-ins of STM images). The intravalley scattering induced by three of the defects (1, 3, and 4) is evident from the long wavelength patterns surrounding these defects. The intervalley scattering appears in the FFT of Figure 4a, shown in Figure 4b as small hollow pockets³² (one of them is boxed in red and shown in greater detail in the inset), while the brightest spots correspond to the atomic lattice (Bragg peaks). The origin of the triangular shape of these hollow pockets is discussed in detail in ref 32. Briefly, it is determined by the joint density of states between adjacent valleys, as schematized in the middle inset of Figure 4b, and its triangular shape is dictated by the strong trigonal warping in BLG. We also highlight the intravalley scattering pattern in the blue-boxed inset of Figure 4b. To study the spatial distribution of the intervalley scattering, we superpose a 256×256 grid on the image in Figure 4a and for each point of this grid, we consider an associated $2.5 \times 2.5 \text{ nm}^2$ window (corresponding to 32×32 pixels). For each of these windows, we then compute the FFT and evaluate the intensity ratio between the intervalley

scattering features and the lattice features (further detail on this method is given in the Supporting Information, section 9).

The result of this analysis is shown in Figure 4c. Several observations can be made. The intervalley scattering at the location of the defect is strong for defects located on the top layer (defects 3 and 4). Although both lie in the top layer, the intervalley scattering induced by defect 4 is significantly more intense than that by defect 3. In addition, the intervalley scattering at the defect location is more acute for defect 4 and it extends significantly further away from the defect than for defect 3. For defect 4, the intervalley scattering extends about 15 nm away from the defect.

Interestingly, the intensity of the intervalley scattering for both defects 3 and 4 (Figure 4c) seems to mimic the intravalley wavelike pattern visible in Figure 4a. This is especially visible around defect 4 in Figure 4c, where a clear wave-like pattern with long wavelength surrounds the defect. A closer examination reveals that the wavelength of the pattern observed in the intervalley (λ_{inter}) scattering map (Figure 4c) is 2 times shorter than the wavelength of the intravalley pattern (λ_{intra}) observed in Figure 4a (~ 6.5 nm vs ~ 13 nm, respectively).

The origin of the observed different wavelengths related to the inter- and intravalley scattering patterns is shown in the insets of Figure 4b. The widths of both patterns are roughly equal (and equal to $4q_F$, with $q_F \approx 0.025 \text{ \AA}^{-1}$ in this case) and are determined by the corresponding extreme scattering vectors, as schematized in the middle inset of Figure 4b.^{23,29} However, in the case of intervalley scattering, the wavelength observed is $\lambda_{\text{inter}} \sim 2\pi/(4q_F)$, corresponding to the difference between the two extreme scattering vectors (see the two red vectors in the red-boxed inset in Figure 4b). In the case of intravalley scattering, the wavelength observed is $\lambda_{\text{intra}} \sim 2\pi/(2q_F)$, corresponding to a wavevector whose length is half the intravalley pattern diameter (see the blue arrow in the blue-framed inset in Figure 4b). This difference is due to the fact that the observed intervalley scattering is caused by beating between the two red vectors (see red-boxed inset in Figure 4b), whereas the observed intravalley scattering is caused by the scattering vectors themselves (such as the blue vector in Figure 4b). Further details on this are provided in the Supporting Information, section 10.

■ INFLUENCE OF THE NATIVE DOPANTS ON THE ELECTRONIC TRANSPORT PROPERTIES OF BLG

Finally, we evaluate the implications of our discovery of native dopants in graphite for the electronic transport properties of BLG, using Boltzmann transport theory. The dopants are modeled as short-range scatterers with a typical potential strength $u = -10$ eV and areal density $n_{\text{dop}} = 10^9 \text{ cm}^{-2}$ (per layer) equally distributed over the A–B sublattices (Figure 3a), as per the QPI simulations above. The longitudinal dc conductivity (σ_{xx}) is obtained via the exact solution of the linearized Boltzmann transport equation within a continuum two-band model of Bernal-stacked BLG (assuming no bulk band gap; this is reasonable since the model is valid only far from the CNP), which captures the essential aspects of electronic transport at low energies; see Supporting Information section XI. In the zero-temperature limit, we obtain

$$\sigma_{xx} = \frac{2e^2}{h} v_F k_F \tau_{\parallel}$$

with k_F the Fermi wavevector, $v_F = 2k_F\beta/\hbar$ the Fermi velocity, and

$$\tau_{\parallel} = \hbar \left[1 + \left(\frac{8\beta}{A_{\text{uc}} u} \right)^2 \right] / (4n_{\text{dop}}\beta)$$

the transport time. Here, $\beta = v^2\hbar^2/t_{\perp}$ (with t_{\perp} the interlayer hopping integral and $v \approx 10^6$ m/s the bare quasiparticle velocity) and A_{uc} denotes the unit cell area. We note that σ_{xx} has little sensitivity to thermal fluctuations provided the Fermi energy is much greater than $k_B T$. The electron mobility is given by $\mu_e = \sigma_{xx}/(en_e)$, with $n_e = \pi k_F^2$ the charge carrier density. For typical material parameters^{32,43} (i.e., $\gamma_1 \approx 0.42$ eV and $A_{\text{uc}} \approx 1.0 \text{ nm}^2$) we find $\mu_e \approx 3.1 \times 10^6$ (cm²/V)/s, which is consistent with the highest reported values for hBN-encapsulated^{44,45} or suspended^{46–48} devices. Because the estimated mobility is 1 order of magnitude higher than the theoretical upper limit set by acoustic phonon scattering,^{49,50} it is important to assess the crossover between impurity-scattering and intrinsic phonon-limited mobility. The mobility as a function of temperature for moderate carrier density is shown in Figure 5, where the extrinsic and intrinsic (acoustic

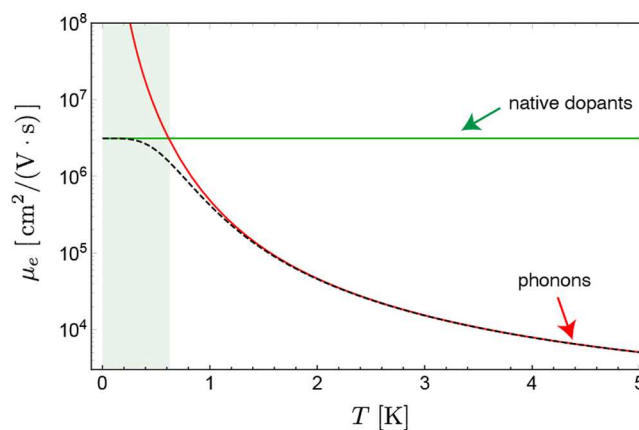


Figure 5. Calculated temperature dependence of carrier mobility in BLG for a dopant concentration of $1 \times 10^9 \text{ cm}^{-2}$. Solid lines show the native-dopant-scattering (green) and acoustic-phonon-scattering limited (red) mobility calculated within the framework of the Boltzmann transport theory. The total charge carrier mobility estimated using Matthiessen's rule is also shown (dashed line). The charge carrier density is fixed at $n_e = 5 \times 10^{12} \text{ cm}^{-2}$ (for other parameters see the main text). Details on the intrinsic phonon-limited mobility calculation are given in Supporting Information, section XI. Shaded green area indicates temperature region where scattering from native dopants is dominant.

phonon) mobilities are compared. Our calculations show that for temperatures below 1 K, the carrier mobility is essentially limited by extrinsic scattering (from native dopants). This holds for a large window of charge carrier densities $n_e \in [10^{11}, 10^{13}]$ (cm⁻²), with the crossover moving toward slightly higher temperatures in more defective samples (e.g., for $n_{\text{dop}} = 10^{11} \text{ cm}^{-2}$, the extrinsic mechanism is found to dominate the electronic transport for $T \lesssim 2$ K). The calculation of the phonon-limited mobility follows ref 49 and for completeness is outlined in Supporting Information, section XI.

CONCLUSION

We have presented STM data that unambiguously demonstrates the presence of native defects in graphite commonly used to make graphene devices. We have further characterized thoroughly the effects of these defects on the electronic properties of BLG. T-matrix calculations reproduced well the gate-dependent reciprocal-space QPI signatures observed experimentally, which are not captured by simple band structure arguments. We have also presented a new method for studying the spatial dependence of intervalley scattering. We have further presented Boltzmann transport calculations predicting that the conductivity of BLG at low temperature (<1 K) and moderate to high carrier density is limited by extrinsic scattering induced by native defects. We expect that the effects discussed in this work will play an important role in other graphene systems, including flatbands systems (bilayer, trilayer, double bilayer, etc.).^{51–58} Extending the methods presented here to these systems should readily reveal the effects of native defects on the exotic correlated states in the magic-angle systems.

METHODS

Sample Fabrication. The graphite (“Flaggy Flakes” and “Graphenium Flakes” from NGS Naturgraphit) sample was exfoliated *in situ* and introduced in the STM within seconds after the exfoliation. The graphene (bilayer and multilayers) sheets were stacked on hBN using a standard polymer-based transfer method.⁵⁹ A graphene flake exfoliated on a methyl methacrylate (MMA) substrate was mechanically placed on top of a 20–50 nm thick hBN flake that rests on a SiO₂/Si²⁺ substrate where the oxide is 285 nm thick. Subsequent solvent baths dissolve the MMA scaffold. After the graphene/hBN heterostructure is assembled, an electrical contact to graphene is made by thermally evaporating 7 nm of Cr and 200 nm of Au using a metallic stencil mask. The single-terminal device is then annealed in forming gas (Ar/H₂) for 6 h at 400 °C to reduce the amount of residual polymer left after the graphene transfer. To further clean the surface of the sample, the heterostructure is mechanically cleaned using an AFM.^{60,61} Finally, the heterostructure is annealed under UHV at 400 °C for 7 h before being introduced into the STM chamber.

STM Measurements. The STM measurements were conducted in ultrahigh vacuum with pressures better than 1×10^{-10} mbar at 4.8 K in a Createc LT-STM. The bias is applied to the sample with respect to the tip. The tips were electrochemically etched tungsten tips, which were calibrated against the Shockley surface state of Au(111) prior to measurements. The STM images presented in the main text and their FFTs were treated with Igor Pro. WSxM⁶² was also used for data presented in the [Supporting Information](#).

ASSOCIATED CONTENT

Supporting Information

The Supporting Information is available free of charge at <https://pubs.acs.org/doi/10.1021/acs.nanolett.1c01442>.

I, Atomic-scale images of defects in exfoliated graphite and in graphene devices; II, concentration of defects; III, extraction of the gap and the electronic doping for the BLG device for each gate voltage; IV, real space imaging of native defects in BLG/hBN devices; V, STM topographic map and dI/dV_s maps at lower current; VI, dependence of the real-space and reciprocal space T-

matrix results on the onsite potential of the defects; VII, joint density of states (jDOS); VIII, zoom-ins around the defects from [Figure 4](#) of the main text; IX, details of the computation of the intervalley scattering map shown in [Figure 4c](#) of the main text; X, wavelength of the intervalley and intravalley patterns observed in [Figure 4](#) of the main text; XI, Boltzmann transport theory ([PDF](#))

AUTHOR INFORMATION

Corresponding Authors

Frédéric Joucken – Department of Physics, University of California, Santa Cruz, California 95064, United States; Department of Physics, Arizona State University, Tempe, Arizona 85287, United States; orcid.org/0000-0002-9056-0081; Email: frederic.joucken@gmail.com

Cristina Bena – Institut de Physique Théorique, Université Paris Saclay, CEA CNRS, 91190 Gif-sur-Yvette, France; Email: cristina.bena@ipht.fr

Jairo Velasco Jr. – Department of Physics, University of California, Santa Cruz, California 95064, United States; orcid.org/0000-0002-3493-1095; Email: jvelasc5@ucsc.edu

Authors

Zhehao Ge – Department of Physics, University of California, Santa Cruz, California 95064, United States

Eberth Quezada-Lopez – Department of Physics, University of California, Santa Cruz, California 95064, United States

Sarah Pinon – Institut de Physique Théorique, Université Paris Saclay, CEA CNRS, 91190 Gif-sur-Yvette, France

Vardan Kaladzhyan – Department of Physics, University of Basel, CH-4056 Basel, Switzerland

Takashi Taniguchi – International Center for Materials Nanoarchitectonics, National Institute for Materials Science, Tsukuba 305-0044, Japan; orcid.org/0000-0002-1467-3105

Kenji Watanabe – Research Center for Functional Materials, National Institute for Materials Science, Tsukuba 305-0044, Japan; orcid.org/0000-0003-3701-8119

Aires Ferreira – Department of Physics and York Centre for Quantum Technologies, University of York, York YO10 SDD, United Kingdom

Complete contact information is available at: <https://pubs.acs.org/doi/10.1021/acs.nanolett.1c01442>

Author Contributions

F.J. discovered the native defects. F.J. carried out the STM measurements. Z.G., E.Q.-L., and F.J. fabricated the graphene on hBN heterostructures. C.B., S.P., and V.K. performed the T-matrix calculations. F.J. carried out the tight-binding calculations. T.T. and K.W. synthesized the hBN crystals. F.J. and C.B. analyzed the data. A.F. carried out the theoretical electronic transport analysis. J.V.J. supervised the STM measurements and the sample fabrication. F.J., A.F., and J.V.J. wrote the manuscript with input from all coauthors.

Funding

J.V.J. acknowledges support from the National Science Foundation under Award DMR-1753367 and the Army Research Office under Contract W911NF-17-1-0473. K.W. and T.T. acknowledge support from the Elemental Strategy Initiative conducted by the MEXT, Japan, Grant JPMXP0112101001 and JSPS KAKENHI Grant

JP20H00354. A.F. acknowledges financial support from the Royal Society through a Royal Society University Research Fellowship.

Notes

The authors declare no competing financial interest.

ACKNOWLEDGMENTS

We thank David Goldhaber-Gordon and François Ducastelle for useful discussions.

REFERENCES

- (1) Novoselov, K. S.; Geim, A. K.; Morozov, S. V.; Jiang, D.; Katsnelson, M. I.; Grigorieva, I. V.; Dubonos, S. V.; Firsov, A. A. Two-Dimensional Gas of Massless Dirac Fermions in Graphene. *Nature* **2005**, *438* (7065), 197–200.
- (2) Tan, Y.-W.; Zhang, Y.; Bolotin, K.; Zhao, Y.; Adam, S.; Hwang, E. H.; Das Sarma, S.; Stormer, H. L.; Kim, P. Measurement of Scattering Rate and Minimum Conductivity in Graphene. *Phys. Rev. Lett.* **2007**, *99* (24), 246803.
- (3) Miao, F.; Wijeratne, S.; Zhang, Y.; Coskun, U. C.; Bao, W.; Lau, C. N. Phase-Coherent Transport in Graphene Quantum Billiards. *Science* **2007**, *317* (5844), 1530–1533.
- (4) Adam, S.; Hwang, E. H.; Galitski, V. M.; Das Sarma, S. A Self-Consistent Theory for Graphene Transport. *Proc. Natl. Acad. Sci. U. S. A.* **2007**, *104* (47), 18392–18397.
- (5) Chen, J.-H.; Jang, C.; Adam, S.; Fuhrer, M. S.; Williams, E. D.; Ishigami, M. Charged-Impurity Scattering in Graphene. *Nat. Phys.* **2008**, *4* (5), 377–381.
- (6) Bolotin, K. I.; Sikes, K. J.; Hone, J.; Stormer, H. L.; Kim, P. Temperature-Dependent Transport in Suspended Graphene. *Phys. Rev. Lett.* **2008**, *101* (9), 96802.
- (7) Du, X.; Skachko, I.; Barker, A.; Andrei, E. Y. Approaching Ballistic Transport in Suspended Graphene. *Nat. Nanotechnol.* **2008**, *3* (8), 491–495.
- (8) Mayorov, A. S.; Gorbachev, R. V.; Morozov, S. V.; Britnell, L.; Jalil, R.; Ponomarenko, L. A.; Blake, P.; Novoselov, K. S.; Watanabe, K.; Taniguchi, T.; et al. Micrometer-Scale Ballistic Transport in Encapsulated Graphene at Room Temperature. *Nano Lett.* **2011**, *11* (6), 2396–2399.
- (9) Castro, E. V.; Ochoa, H.; Katsnelson, M. I.; Gorbachev, R. V.; Elias, D. C.; Novoselov, K. S.; Geim, A. K.; Guinea, F. Limits on Charge Carrier Mobility in Suspended Graphene Due to Flexural Phonons. *Phys. Rev. Lett.* **2010**, *105* (26), 266601.
- (10) Park, C.-H.; Bonini, N.; Sohler, T.; Samsonidze, G.; Kozinsky, B.; Calandra, M.; Mauri, F.; Marzari, N. Electron-Phonon Interactions and the Intrinsic Electrical Resistivity of Graphene. *Nano Lett.* **2014**, *14* (3), 1113–1119.
- (11) Couto, N. J. G.; Engels, S.; Taniguchi, T.; Guinea, F.; Stampfer, C.; Watanabe, K.; Morpurgo, A. F.; Costanzo, D.; Ki, D.-K. Random Strain Fluctuations as Dominant Disorder Source for High-Quality On-Substrate Graphene Devices. *Phys. Rev. X* **2014**, *4* (4), 041019.
- (12) Engels, S.; Terrés, B.; Epping, A.; Khodkov, T.; Watanabe, K.; Taniguchi, T.; Beschoten, B.; Stampfer, C. Limitations to Carrier Mobility and Phase-Coherent Transport in Bilayer Graphene. *Phys. Rev. Lett.* **2014**, *113* (12), 126801.
- (13) Hwang, E. H.; Das Sarma, S. Impurity-Scattering-Induced Carrier Transport in Twisted Bilayer Graphene. *Phys. Rev. Res.* **2020**, *2* (1), 13342.
- (14) Yudhistira, I.; Chakraborty, N.; Sharma, G.; Ho, D. Y. H.; Laksono, E.; Sushkov, O. P.; Vignale, G.; Adam, S. Gauge-Phonon Dominated Resistivity in Twisted Bilayer Graphene near Magic Angle. *Phys. Rev. B: Condens. Matter Mater. Phys.* **2019**, *99* (14), 140302.
- (15) Ramires, A.; Lado, J. L. Impurity-Induced Triple Point Fermions in Twisted Bilayer Graphene. *Phys. Rev. B: Condens. Matter Mater. Phys.* **2019**, *99* (24), 245118.
- (16) Atamny, F.; Baiker, A.; Schlögl, R. Atomic Resolution of Defects in Graphite Studied by STM. *Fresenius' J. Anal. Chem.* **1997**, *358* (1), 344–348.
- (17) Osing, J.; Shvets, I. V. Bulk Defects in Graphite Observed with a Scanning Tunneling Microscope. *Surf. Sci.* **1998**, *417* (1), 145–150.
- (18) Pong, W.-T.; Durkan, C. A Review and Outlook for an Anomaly of Scanning Tunneling Microscopy (STM): Superlattices on Graphite. *J. Phys. D: Appl. Phys.* **2005**, *38* (21), R329–R355.
- (19) Simonis, P.; Goffaux, C.; Thiry, P. A.; Biro, L. P.; Lambin, P.; Meunier, V. STM Study of a Grain Boundary in Graphite. *Surf. Sci.* **2002**, *511* (1), 319–322.
- (20) Červenka, J.; Katsnelson, M. I.; Flipse, C. F. J. Room-Temperature Ferromagnetism in Graphite Driven by Two-Dimensional Networks of Point Defects. *Nat. Phys.* **2009**, *5* (11), 840–844.
- (21) Telling, R. H.; Heggie, M. I. Radiation Defects in Graphite. *Philos. Mag.* **2007**, *87* (31), 4797–4846.
- (22) Kondo, T.; Honma, Y.; Oh, J.; Machida, T.; Nakamura, J. Edge States Propagating from a Defect of Graphite: Scanning Tunneling Spectroscopy Measurements. *Phys. Rev. B: Condens. Matter Mater. Phys.* **2010**, *82* (15), 153414.
- (23) Rutter, G. M.; Crain, J. N.; Guisinger, N. P.; Li, T.; First, P. N.; Stroscio, J. A. Scattering and Interference in Epitaxial Graphene. *Science* **2007**, *317* (5835), 219–222.
- (24) Ugeda, M. M.; Fernández-Torre, D.; Brihuega, I.; Pou, P.; Martínez-Galera, A. J.; Pérez, R.; Gómez-Rodríguez, J. M. Point Defects on Graphene on Metals. *Phys. Rev. Lett.* **2011**, *107* (11), 116803.
- (25) Cockayne, E.; Rutter, G. M.; Guisinger, N. P.; Crain, J. N.; First, P. N.; Stroscio, J. A. Grain Boundary Loops in Graphene. *Phys. Rev. B: Condens. Matter Mater. Phys.* **2011**, *83* (19), 195425.
- (26) Simon, L.; Bena, C.; Vonau, F.; Aubel, D.; Nasrallah, H.; Habar, M.; Peruchetti, J. C. Symmetry of Standing Waves Generated by a Point Defect in Epitaxial Graphene. *Eur. Phys. J. B* **2009**, *69* (3), 351–355.
- (27) Zhang, Y.; Brar, V. W.; Girit, C.; Zettl, A.; Crommie, M. F. Origin of Spatial Charge Inhomogeneity in Graphene. *Nat. Phys.* **2009**, *5*, 722.
- (28) Brihuega, I.; Mallet, P.; Bena, C.; Bose, S.; Michaelis, C.; Vitali, L.; Varchon, F.; Magaud, L.; Kern, K.; Veuillen, J. Y. Quasiparticle Chirality in Epitaxial Graphene Probed at the Nanometer Scale. *Phys. Rev. Lett.* **2008**, *101* (20), 206802.
- (29) Mallet, P.; Brihuega, I.; Bose, S.; Ugeda, M. M.; Gómez-Rodríguez, J. M.; Kern, K.; Veuillen, J. Y. Role of Pseudospin in Quasiparticle Interferences in Epitaxial Graphene Probed by High-Resolution Scanning Tunneling Microscopy. *Phys. Rev. B: Condens. Matter Mater. Phys.* **2012**, *86* (4), 045444.
- (30) Wong, D.; Velasco, J.; Ju, L.; Lee, J.; Kahn, S.; Tsai, H.-Z.; Germany, C.; Taniguchi, T.; Watanabe, K.; Zettl, A.; et al. Characterization and Manipulation of Individual Defects in Insulating Hexagonal Boron Nitride Using Scanning Tunneling Microscopy. *Nat. Nanotechnol.* **2015**, *10* (11), 949–953.
- (31) Halbertal, D.; Ben Shalom, M.; Uri, A.; Bagani, K.; Meltzer, A. Y.; Marcus, I.; Myasoedov, Y.; Birkbeck, J.; Levitov, L. S.; Geim, A. K.; Zeldov, E. Imaging Resonant Dissipation from Individual Atomic Defects in Graphene. *Science* **2017**, *358* (6368), 1303–1306.
- (32) Joucken, F.; Ge, Z.; Quezada-López, E. A.; Davenport, J. L.; Watanabe, K.; Taniguchi, T.; Velasco, J. Determination of the Trigonal Warping Orientation in Bernal-Stacked Bilayer Graphene via Scanning Tunneling Microscopy. *Phys. Rev. B: Condens. Matter Mater. Phys.* **2020**, *101* (16), 161103.
- (33) Bena, C. Effect of a Single Localized Impurity on the Local Density of States in Monolayer and Bilayer Graphene. *Phys. Rev. Lett.* **2008**, *100* (7), 76601.
- (34) Deshpande, A.; Bao, W.; Zhao, Z.; Lau, C. N.; LeRoy, B. J. Mapping the Dirac Point in Gated Bilayer Graphene. *Appl. Phys. Lett.* **2009**, *95* (24), 243502.
- (35) Yankowitz, M.; Wang, J. I.-J.; Li, S.; Birdwell, A. G.; Chen, Y.-A.; Watanabe, K.; Taniguchi, T.; Quek, S. Y.; Jarillo-Herrero, P.;

LeRoy, B. J. Band Structure Mapping of Bilayer Graphene via Quasiparticle Scattering. *APL Mater.* **2014**, *2* (9), 092503.

(36) Holdman, G. R.; Krebs, Z. J.; Behn, W. A.; Smith, K. J.; Watanabe, K.; Taniguchi, T.; Brar, V. W. Dynamic Band Structure and Capacitance Effects in Scanning Tunneling Spectroscopy of Bilayer Graphene. *Appl. Phys. Lett.* **2019**, *115* (18), 181601.

(37) Kohsaka, Y.; Machida, T.; Iwaya, K.; Kanou, M.; Hanaguri, T.; Sasagawa, T. Spin-Orbit Scattering Visualized in Quasiparticle Interference. *Phys. Rev. B: Condens. Matter Mater. Phys.* **2017**, *95* (11), 115307.

(38) Derry, P. G.; Mitchell, A. K.; Logan, D. E. Quasiparticle Interference from Magnetic Impurities. *Phys. Rev. B: Condens. Matter Mater. Phys.* **2015**, *92* (3), 35126.

(39) Mitchell, A. K.; Fritz, L. Signatures of Weyl Semimetals in Quasiparticle Interference. *Phys. Rev. B: Condens. Matter Mater. Phys.* **2016**, *93* (3), 35137.

(40) Simon, L.; Bena, C.; Vonau, F.; Cranney, M.; Aubel, D. Fourier-Transform Scanning Tunneling Spectroscopy: The Possibility to Obtain Constant-Energy Maps and Band Dispersion Using a Local Measurement. *J. Phys. D: Appl. Phys.* **2011**, *44* (46), 464010.

(41) Zhao, L.; He, R.; Rim, K. T.; Schiros, T.; Kim, K. S.; Zhou, H.; Gutiérrez, C.; Chockalingam, S. P.; Arguello, C. J.; Pálová, L.; et al. Visualizing Individual Nitrogen Dopants in Monolayer Graphene. *Science* **2011**, *333* (6045), 999–1003.

(42) Yan, H.; Liu, C.-C.; Bai, K.-K.; Wang, X.; Liu, M.; Yan, W.; Meng, L.; Zhang, Y.; Liu, Z.; Dou, R.; et al. Electronic Structures of Graphene Layers on a Metal Foil: The Effect of Atomic-Scale Defects. *Appl. Phys. Lett.* **2013**, *103* (14), 143120.

(43) Joucken, F.; Quezada-López, E. A.; Avila, J.; Chen, C.; Davenport, J. L.; Chen, H.; Watanabe, K.; Taniguchi, T.; Asensio, M. C.; Velasco, J. Nanospot Angle-Resolved Photoemission Study of Bernal-Stacked Bilayer Graphene on Hexagonal Boron Nitride: Band Structure and Local Variation of Lattice Alignment. *Phys. Rev. B: Condens. Matter Mater. Phys.* **2019**, *99* (16), 161406.

(44) Maher, P.; Wang, L.; Gao, Y.; Forsythe, C.; Taniguchi, T.; Watanabe, K.; Abanin, D.; Papić, Z.; Cadden-Zimansky, P.; Hone, J.; et al. Tunable Fractional Quantum Hall Phases in Bilayer Graphene. *Science* **2014**, *345* (6192), 61–64.

(45) Bandurin, D. A.; Torre, I.; Kumar, R. K.; Ben Shalom, M.; Tomadin, A.; Principi, A.; Auton, G. H.; Khestanova, E.; Novoselov, K. S.; Grigorieva, I. V.; et al. Negative Local Resistance Caused by Viscous Electron Backflow in Graphene. *Science* **2016**, *351* (6277), 1055–1058.

(46) Bao, W.; Velasco, J.; Zhang, F.; Jing, L.; Standley, B.; Smirnov, D.; Bockrath, M.; MacDonald, A. H.; Lau, C. N. Evidence for a Spontaneous Gapped State in Ultraclean Bilayer Graphene. *Proc. Natl. Acad. Sci. U. S. A.* **2012**, *109* (27), 10802–10805.

(47) Ki, D.-K.; Fal'ko, V. I.; Abanin, D. A.; Morpurgo, A. F. Observation of Even Denominator Fractional Quantum Hall Effect in Suspended Bilayer Graphene. *Nano Lett.* **2014**, *14* (4), 2135–2139.

(48) Mayorov, A. S.; Elias, D. C.; Mucha-Kruczynski, M.; Gorbachev, R. V.; Tudorovskiy, T.; Zhukov, A.; Morozov, S. V.; Katsnelson, M. I.; Geim, A. K.; Novoselov, K. S. Interaction-Driven Spectrum Reconstruction in Bilayer Graphene. *Science* **2011**, *333* (6044), 860–863.

(49) Ochoa, H.; Castro, E. V.; Katsnelson, M. I.; Guinea, F. Temperature-Dependent Resistivity in Bilayer Graphene Due to Flexural Phonons. *Phys. Rev. B: Condens. Matter Mater. Phys.* **2011**, *83* (23), 235416.

(50) Hwang, E. H.; Das Sarma, S. Acoustic Phonon Scattering Limited Carrier Mobility in Two-Dimensional Extrinsic Graphene. *Phys. Rev. B: Condens. Matter Mater. Phys.* **2008**, *77* (11), 115449.

(51) Shi, Y.; Xu, S.; Yang, Y.; Slizovskiy, S.; Morozov, S. V.; Son, S.-K.; Ozdemir, S.; Mullan, C.; Barrier, J.; Yin, J.; et al. Electronic Phase Separation in Multilayer Rhombohedral Graphite. *Nature* **2020**, *584* (7820), 210–214.

(52) Hao, Z.; Zimmerman, A. M.; Ledwith, P.; Khalaf, E.; Najafabadi, D. H.; Watanabe, K.; Taniguchi, T.; Vishwanath, A.; Kim, P. Electric Field-Tunable Superconductivity in Alternating-Twist

Magic-Angle Trilayer Graphene. *Science* **2021**, *371* (6534), 1133–1138.

(53) Wu, S.; Zhang, Z.; Watanabe, K.; Taniguchi, T.; Andrei, E. Y. Chern Insulators, van Hove Singularities and Topological Flat Bands in Magic-Angle Twisted Bilayer Graphene. *Nat. Mater.* **2021**, *20* (4), 488–494.

(54) Choi, Y.; Kim, H.; Peng, Y.; Thomson, A.; Lewandowski, C.; Polski, R.; Zhang, Y.; Arora, H. S.; Watanabe, K.; Taniguchi, T.; et al. Correlation-Driven Topological Phases in Magic-Angle Twisted Bilayer Graphene. *Nature* **2021**, *589* (7843), 536–541.

(55) Zhou, H.; Xie, T.; Ghazaryan, A.; Holder, T.; Ehrets, J. R.; Spanton, E. M.; Taniguchi, T.; Watanabe, K.; Berg, E.; Serbyn, M.; et al. Half and Quarter Metals in Rhombohedral Trilayer Graphene. *arXiv* **2021**, arXiv:2104.00653.

(56) Wong, D.; Nuckolls, K. P.; Oh, M.; Lian, B.; Xie, Y.; Jeon, S.; Watanabe, K.; Taniguchi, T.; Bernevig, B. A.; Yazdani, A. Cascade of Electronic Transitions in Magic-Angle Twisted Bilayer Graphene. *Nature* **2020**, *582* (7811), 198–202.

(57) Cao, Y.; Fatemi, V.; Fang, S.; Watanabe, K.; Taniguchi, T.; Kaxiras, E.; Jarillo-Herrero, P. Unconventional Superconductivity in Magic-Angle Graphene Superlattices. *Nature* **2018**, *556*, 43.

(58) Cao, Y.; Fatemi, V.; Demir, A.; Fang, S.; Tomarken, S. L.; Luo, J. Y.; Sanchez-Yamagishi, J. D.; Watanabe, K.; Taniguchi, T.; Kaxiras, E.; et al. Correlated Insulator Behaviour at Half-Filling in Magic-Angle Graphene Superlattices. *Nature* **2018**, *556*, 80.

(59) Zomer, P. J.; Dash, S. P.; Tombros, N.; van Wees, B. J. A Transfer Technique for High Mobility Graphene Devices on Commercially Available Hexagonal Boron Nitride. *Appl. Phys. Lett.* **2011**, *99* (23), 232104.

(60) Goossens, A. M.; Calado, V. E.; Barreiro, A.; Watanabe, K.; Taniguchi, T.; Vandersypen, L. M. K. Mechanical Cleaning of Graphene. *Appl. Phys. Lett.* **2012**, *100* (7), 073110.

(61) Ge, Z.; Joucken, F.; Quezada, E.; da Costa, D. R.; Davenport, J.; Giraldo, B.; Taniguchi, T.; Watanabe, K.; Kobayashi, N. P.; Low, T.; et al. Visualization and Manipulation of Bilayer Graphene Quantum Dots with Broken Rotational Symmetry and Nontrivial Topology. *Nano Lett.* **2020**, *20* (12), 8682–8688.

(62) Horcas, I.; Fernández, R.; Gómez-Rodríguez, J. M.; Colchero, J.; Gómez-Herrero, J.; Baro, A. M. WSXM: A Software for Scanning Probe Microscopy and a Tool for Nanotechnology. *Rev. Sci. Instrum.* **2007**, *78* (1), 013705.